Research Article

Nano Research
2023, 16(2): 3524–3535

ISSN 1998-0124 CN 11-5974/O4
https://doi.org/10.1007/s12274-022-4900-7

Few-layered MoS_2 anchored on 2D porous C_3N_4 nanosheets for Pt-free photocatalytic hydrogen evolution

Nan Wang, Dongxu Wang, Aiping Wu, Siyu Wang, Zhihui Li, Chengxu Jin, Youming Dong, Fanyi Kong, Chungui Tian (✉), and Honggang Fu (✉)

Key Laboratory of Functional Inorganic Material Chemistry, Ministry of Education of the People's Republic of China, Heilongjiang University, Harbin 150080, China

Received: 30 June 2022 / **Revised:** 10 August 2022 / **Accepted:** 11 August 2022

ABSTRACT

The Pt-free photocatalytic hydrogen evolution (PHE) has been the focus in the photocatalytic field. The catalytic system with the large accessible surface and good mass-transfer ability, as well as the intimate combination of co-catalyst with semiconductor is promising for the promotion of the application. Here, we have reported the design of the two-dimensional (2D) porous C_3N_4 nanosheets (PCN NS) intimately combined with few-layered MoS_2 for the high-effective Pt-free PHE. The PCN NS were synthesized based on peeling the melamine–cyanuric acid precursor (MC precursor) by the triphenylphosphine (TP) molecular followed by the calcination, mainly due to the matched size of the (100) plane distance of the precursor (0.8 nm) and the height of TP molecular. The porous structure is favorable for the mass-transfer and the 2D structure having large accessible surface, both of which are positive to promote the photocatalytic ability. The few-layered MoS_2 are grown on PCN to give 2D MoS_2/PCN composites based on anchoring phosphomolybdic acid (PMo_{12}) cluster on polyetherimide (PEI)-modified PCN followed by the vulcanization. The few-layered MoS_2 have abundant edge active sites, and its intimate combination with porous PCN NS is favorable for the faster transfer and separation of the electrons. The characterization together with the advantage of 2D porous structure can largely promote the photocatalytic ability. The MoS_2/PCN showed good PHE activity with the high hydrogen production activity of 4,270.8 $\mu mol \cdot h^{-1} \cdot g^{-1}$ under the simulated sunlight condition (AM1.5), which was 7.9 times of the corresponding MoS_2/bulk C_3N_4 and 12.7 times of the 1 wt.% Pt/bulk C_3N_4. The study is potentially meaningful for the synthesis of PCN-based catalytic systems.

KEYWORDS

two-dimensional porous C_3N_4 nanosheets, photocatalysis, few-layered MoS_2, Pt-free hydrogen evolution

1 Introduction

The effective utilization of solar energy is key to relieving energy and environmental problems. The photocatalytic process driven by solar light can convert solar energy into hydrogen in a "green" way. The photocatalysts with a suitable band gap, abundant active sites, and short carrier diffusion distance should be developed to realize effective conversion [1, 2]. Among many well-known photocatalysts, the graphitic carbon nitride (g-C_3N_4) has attracted wide attention because of its ability to utilize visible light and safety [3, 4]. The performance of the g-C_3N_4 can be governed by the band-gap, the numbers of the active sites and the contact with the reagents, which pushed the intensive study on the design of g-C_3N_4 with well-defined micro-structures to boost the performance [5, 6]. Morphology engineering has been promising because it can improve one or several favorable factors simultaneously [7–11]. Typically, the hollow g-C_3N_4 spheres have shown improved catalytic ability due to their large specific surface area inside and outside favorable to promote the shuttle of carriers [12, 13]. The C_3N_4 quantum dots showed the improved performance, which can be related to the large number of edge active sites and shorter transmission path of the carriers [14].

The two-dimensional (2D) g-C_3N_4 is of promising due to their characterization of large accessible specific surfaces and exposing plentiful active sites [15–18]. The 2D structure can more effectively combine with 2D structure (for example MoS_2, a well-known non-Pt co-catalyst), being favorable to promoting the catalytic performance [19, 20]. The g-C_3N_4 is a layered structure composed of C-N rings bonded by strong covalent bonding, in which the layers are combined by weak van der Waals interactions [21–23]. Thus, the "top–down" exfoliation of bulk C_3N_4 (BCN), just like the graphene preparation from the graphite [24], is frequently used to prepare g-C_3N_4 sheets but suffered from the strict synthetic conditions (sometimes strong oxidants are needed), and the formation of the thick layer [25–27]. In contrast, the "bottom–up" assembly is considered as potential strategy to prepare the 2D g-C_3N_4 [28, 29]. The core of the strategy is a construction of the layered lamellar precursor followed by well-designed post-treatment. The choice of molecules which have strong interaction with the layered precursor would be important to synthesize the 2D g-C_3N_4.

Our previous works proved the preparation of the complex composed of layered stacked melamine–cyanuric acid coordination layers with the inter-plane distance of 0.8 nm [30]. In

Address correspondence to Chungui Tian, chunguitianhq@163.com, tianchungui@hlju.edu.cn; Honggang Fu, fuhg@vip.sina.com, fuhg@hlju.edu.cn

principle, a molecular with matched size close to inter-plane distance can potentially peel the precursor to give a 2D layer. The triphenylphosphine (TP), composed of sp^3 hybridized phosphorus coordinated with three phenyl groups, has a tetrahedral molecular spatial structure. The molecular structure of TP is shown in Fig. S1 in the Electronic Supplementary Material (ESM), its height of 0.8 nm is close to the distance of the (100) crystal planes of the precursor. Also, there is π–π interaction between the benzene ring in TP with the precursor layers [31, 32]. The characteristics suggest the potential of TP as an effective "peeling" reagent for the synthesis of 2D g-C_3N_4. Here, the precursor with layered stacked structure was firstly treated by TP molecules assisted by vacuum. The process makes the "expansion" of the precursor along (002) direction and the formation of the like-accordion structure. Subsequently, the controllable heating leads to the formation of 2D porous ultra-thin g-C_3N_4 nanosheets (PCN NS). The PCN NS has plentiful pores with a large surface area (168.75 $m^2 \cdot g^{-1}$), much higher than the BCN (4.56 $m^2 \cdot g^{-1}$) and C_3N_4 tubes (22.95 $m^2 \cdot g^{-1}$) directly derived from the precursor [30]. Also, there is presence of plentiful nitrogen defects on the PCN NS, which can furtherly facilitate the separation and transfer of photogenerated carriers in π conjugate plane. The 2D PCN NS was combined with few-layered, well-dispersed MoS_2 characterized by the abundant edge active sites. The 2D MoS_2/PCN showed good photocatalytic hydrogen evolution (PHE) activity with the high hydrogen production activity of 4,270.8 $\mu mol \cdot h^{-1} \cdot g^{-1}$ under the simulated sunlight condition (AM1.5), which was 7.9 times the corresponding MoS_2/BCN. The good activity was related to the tight binding of few-layered MoS_2 with abundant edge active sites and porous PCN NS for faster electron transfer and effective separation, as well as the porous structure for good mass transfer and 2D sheets with a large accessible surface.

2 Experimental

2.1 Materials and chemicals

Melamine ($C_3H_6N_6$), phosphoric acid (H_3PO_4), phosphomolybdic acid ($H_3PMo_{12}O_{40}$, PMo_{12}), polyetherimide ($(C_2H_5N)_n$, PEI), TP ($C_{18}H_{15}P$), and ethanol (C_2H_5OH) were all purchased from Aladdin Chemical Reagent Co, Ltd. Polyethyleneimine was purchased from Sigma–Aldrich. All of the reagents were used without any further purification.

2.2 Synthesis of the photocatalysts

2.2.1 Preparation of 2D PCN NS

A supramolecular precursor with the layered stacked structure was firstly synthesized according to our previous work [30]. The PCN NS were synthesized based on the vacuum-assisted peeling of the precursor by the TP followed by the controllable calcination. First, the 2.4 g precursor was added into an empty flask, which was sealed with a separatory funnel and connected to a vacuum pump. After vacuuming for two hours, 20 mL of ethanol solution of TP was added drop by drop through a separating funnel under stirring within the period of 5 min. After further stirring for 30 min under vacuum conditions, the solid was separated by the centrifugation, and washed several times with ethanol and dried by vacuum freeze–drying. The solids were heated to 500 °C in a muffle furnace with a heating rate of 1.5 $°C \cdot min^{-1}$ and kept at this temperature for 2 h, and the final PCN NS were obtained.

2.2.2 Preparation of BCN

2 g melamine powder was put into a porcelain crucible, and then heated to 500 °C in a muffle furnace with a heating rate of 1.5 $°C \cdot min^{-1}$ and kept at this temperature for 2 h. After cooling to room temperature, the solids (BCN) were obtained [1, 3, 8].

2.2.3 Preparation of MoS_2/PCN NS

The few-layered MoS_2 was anchored on PCN NS based on the coupling of PMo_{12} clusters with PCN NS by PEI. As we all know, PEI was a common positively charged polymer, in which a large number of amine groups can be combined with negatively charged colloids and ions. Therefore, after mixing, the positively charged PEI could coordinate with the $-NH_2$ group carried by the PCN NS through the amine, and bond with the PCN NS to form a positively charged PEI-PCN NS. In particular, the 100 mg of PCN NS was dispersed in 50 mL deionized (DI) water followed by dropwise adding 5 mL of PEI solution (4 $mg \cdot mL^{-1}$) under stirring. After the dispersion was stirred for 24 h, the excess PEI was removed by repeated centrifugation (4,000 rpm, 3 min) and washing cycles (denoted as PEI-PCN NS). The PEI-PCN NS was dispersed in DI water. The PMo_{12} (0.02 g) in DI water (5 mL) was added dropwise into the 50 mL of PEI-PCN NS solution (2 $mg \cdot mL^{-1}$) under vigorously stirring. After stirring for 24 h, the solid was collected by centrifugation, and washed repeatedly with DI water and alcohol. After drying at 60 °C for 8 h, the PMo_{12}/PEI-PCN NS was obtained.

For the synthesis of MoS_2/PCN NS, two porcelain crucibles separately containing the sulfur powder and the PMo_{12}/PEI-PCN NS were placed at a heating zone of the two-zone tube furnace with containing-S porcelain crucibles at the upstream side. The temperature for both zones was heated to 450 °C with a heating rate of 5 $°C \cdot min^{-1}$ under N_2 flow (50 sccm) and maintained at 450 °C for 2 h. After slowly cooling to room temperature, the MoS_2/PCN NS (P) (the "P" indicates the sample from the "PEI" coupling route) was formed. The amount of Mo loading on PCN NS was about 4% by thermogravimetric test.

For comparison, the MoS_2/PCN NS (I) (without the use of PEI as a coupling agent) and MoS_2/BCN (I) were also prepared. Typically, the 100 mg of PCN NS (or BCN) was dispersed in 50 mL DI water. Then, 0.004g PMo_{12} in DI water (5 mL) was added dropwise into the PCN NS solution of 50 mL (2 $mg \cdot mL^{-1}$) under vigorously stirring. After stirring until the sample was dry, the PMo_{12}/PCN NS (PMo_{12}/BCN) was obtained. After that, the vulcanization process of PMo_{12}/BCN and PMo_{12}/PCN NS was similar to that of the MoS_2/ PCN NS (P), and corresponding MoS_2/PCN NS (I) and MoS_2/BCN (I) were obtained.

2.3 Characterization

X-ray diffraction (XRD) patterns were obtained on a Bruker D8 diffractometer with nickel-filtered Cu Kα radiation (λ = 0.15405 nm, 40 kV, 100 mA). The structure of the samples was characterized using a Hitachi S-4800 field emission scanning electron microscopy (SEM) operating at 15 kV and JEM-F200 transmission electron microscopy (TEM, JEOL) with an acceleration voltage of 200 kV. Energy dispersive X-ray (EDX) spectroscopy and elemental mapping were performed on the TEM. Fourier transform infrared spectroscopy (FTIR) was recorded on a Perkin–Elmer Spectrum One spectrometer using potassium bromide (KBr) pellets. The photoluminescence (PL) spectra were recorded with a Hitachi F-4600 fluorescence spectrophotometer at room temperature. Surface areas were measured using an ASAP 2420 (Micro-metrics Instruments) surface area analyzer using the Brunauer–Emmett–Teller (BET) method. Ultraviolet–visible (UV–vis) absorption spectroscopy was recorded using a UV–vis spectrophotometer (Shimadzu UV-2550). X-ray photoelectron spectroscopy (XPS) analysis was performed on a VG ESCALAB MK II with an Mg Kα (1,253.6 eV) achromatic X-ray source. The thickness of samples was analyzed

by a Multimode Nanoscope VIII instrument (Bruker) atomic force microscopy (AFM). The electron paramagnetic resonance (EPR) of the samples was performed by a Bruker EMX plus model spectrometer at room temperature. Zeta potential measurements were obtained by Malvern Zetasizer Nano ZS90. In this case, 10 mg of the sample was dispersed in 20 mL of DI water by sonication at room temperature.

2.4 Photoelectrochemical test

Photoelectrochemical measurements were performed by using a BAS100B electrochemical analyzer (Bioanalytical Systems Inc., USA) in a standard three-compartment cell. A Pt plate and a saturated Ag/AgCl electrode were used as the counter and reference electrodes, respectively. For the working electrodes, a sample (10 mg) was dispersed in ethanol (10 mL) to obtain a slurry. The slurry was coated onto the fluorine-doped tin oxide (FTO) glass substrates and dried in an oven overnight and calcinated at 400 °C (heating rate of 5 °C·min^{-1}) for 60 min under nitrogen flow. The aqueous solution of Na_2SO_4 (0.2 mol·L^{-1}) was used as a supporting electrolyte, which was purged with N_2 for 60 min before measurements. All photoelectrochemical experiments were carried out under AM1.5 irradiation with a power density of 100 mW·cm^{-2}. Linear sweep voltammetry (LSV) measurements were carried out at a scan rate of 10 mV·s^{-1}. Electrochemical impedance spectroscopy (EIS) experiments were conducted in dark. Mott–Schottky plots were collected with a scan rate of 5 mV·s^{-1} at a different frequencies (1.0k, 1.2k, and 1.4k Hz).

2.5 Measurement of PHE

The photocatalytic H_2 evolution reactions were carried out in an online photocatalytic hydrogen production system (AuLight, CEL-SPH2N, Beijing PerfectLight) at 25 °C. A Xenon arc lamp (300 W) with an AM1.5 bandpass filter or cutoff filter (λ > 400 nm) as the light source to trigger the photocatalytic reaction. In a typical experiment, 10 mg of photocatalyst (MoS_2/PCN NS (P), MoS_2/PCN NS and MoS_2/BCN) was suspended in a mixture of 80 mL distilled water and 20 mL methanol in the reaction cell under magnetic stirring. Before the reaction, the mixture was degassed under vacuum to remove O_2 and CO_2. During the reaction process, the evolution gas was observed only under irradiation and analyzed by an online gas chromatograph (GC7900, TCD, molecular sieve 5 Å, Ar carrier, Beijing Keruida Limited)

3 Results and discussion

3.1 Material characterization

The synthesis process of 2D PCN NS is shown in Fig. 1(a). The process starts from the synthesis of the rod-shaped supramolecular precursor with a layered-like stacked structure [30]. The precursor was treated by TP molecular-based on the vacuum-assisted method. The process makes the "expansion" of the precursor along the (002) direction, thus forming the like-accordion structure. Subsequently controlled heating leads to the formation of 2D PCN NS. The plentiful amine groups in PEI can interact with both PMo_{12} and C_3N_4, so they can act as "coupling molecular" for linking the PMo_{12} and g-C_3N_4 [33]. Zeta potential test was conducted on PCN NS and PEI-modified PCN NS respectively. The test results showed that the zeta potential of PCN NS was −17.6 mV and the zeta potential of PEI-PCN NS is 38.8 mV (Fig. S2 in the ESM). So, by using PEI as a coupling agent, the PMo_{12} clusters can be anchored onto PCN NS, and subsequently transformed into few-layered, well-dispersed MoS_2 by the controlled vulcanization.

The precursor shows the hexagonal rod-shaped morphology with a length of 200–500 μm and a diameter of 30–80 μm (Figs. S3(a) and S3(b) in the ESM). The precursor has a layered-like stacked structure as demonstrated by our previous report [30]. As known, the materials with the layered-like structure can be exfoliated by the intercalation to give the 2D structure. So, this layered-like structure of the precursor allows the intercalation of suitable molecules between the layers inspired by previous studies about the graphite, layered double hydroxide (LDH) and MoS_2 [34, 35]. The key is the search for a molecular with matched size close to interlayer spacing and proper interaction with the layer. The TP has a height of 0.8 nm, being close to the distance between the (100) crystal planes of the precursor. Also, it is speculated the presence of strong π–π interaction between the benzene ring in TP and the C-N rings of precursor layers.

Next, we discuss in depth the formation process of 2D PCN NS: Since the TP molecule is a three-dimensional (3D) structure formed by the coordination of sp^3 hybridized phosphorus and three phenyl groups, we believe that the benzene ring in the TP molecule can have a strong interaction with the layered g-C_3N_4 precursor. The interaction helps to peel off the layered precursor into thin sheets. As shown in Figs. S3(c) and S3(d) in the ESM, the hexagonal micro-rods turned into an accordion-like structure after treatment by TP, indicating the strong interaction of TP with the precursor layers (precursor-T). Especially, as shown in Fig. S4 in the ESM, one weak peak located at 28.23° in the precursor become very strong in precursor-T. Other peaks emerged in the precursor almost disappeared in precursor-T, especially those peaks located before 28.23°. The peak located at 28.23° can be indexed in the (002) plane (basic plane) of the precursor. The strong peaks in the precursor-T imply the exfoliation of the precursor along (100) direction. Notably, there is no obvious changes in the peaks in XRD patterns located before 28.23° when the precursor was treated in ethanol (precursor-E). The XRD pattern of precursor-E is similar to that of the samples from directly grinding the precursor. The slight change in the XRD pattern should be attributed to the crack of the precursor into the small grain rather than the exfoliation. The time-dependent experiments verified the gradually expanded and finally exfoliated precursor. The results show the role of TP in the effective exfoliation of the precursor.

The precursor-T is also composed of melamine and cyanuric acid units which are suitable components for the synthesis of g-C_3N_4. So, the precursor-T was heated in the air, just like the general procedure for the preparation of g-C_3N_4. The thermal gravimetric (TG) test (Fig. S5 in the ESM) was firstly carried out to investigate the pyrolysis process of the precursor-T. As shown, the precursor-T began to lose weight at 300 °C, which was attributed to the evaporation of adsorbed molecules on the surface. A significant weight loss is observed in the range of 300–450 °C, which is due to the condensation polymerization of the precursor. During the heating process, the precursor releases NH_3, NO_2, N_2O/CO_2, and other gases, which further promotes its exfoliation into ultra-thin nanosheets and the formation of the pores [23]. By comparison, the precursor without intercalation of TP has a slightly higher weight-loss temperature. As shown in previous work, the decrease in the size can decrease the pyrolysis temperature for the zeolitic imidazolate framework (ZIF)-8 particle and 2D ZIF-67 sheets [36, 37]. So, the lower weight-loss temperature of precursor-T can be related to its thin-sheet structure.

In order to clarify the formation process of the 2D PCN NS, the thermal oxidative exfoliation was further studied. We have found gradual increases in the degree of peeling as the increase of calcination temperature from 350 to 500 °C. Typically, the calcination at the 350 °C can result in the slight expansion of

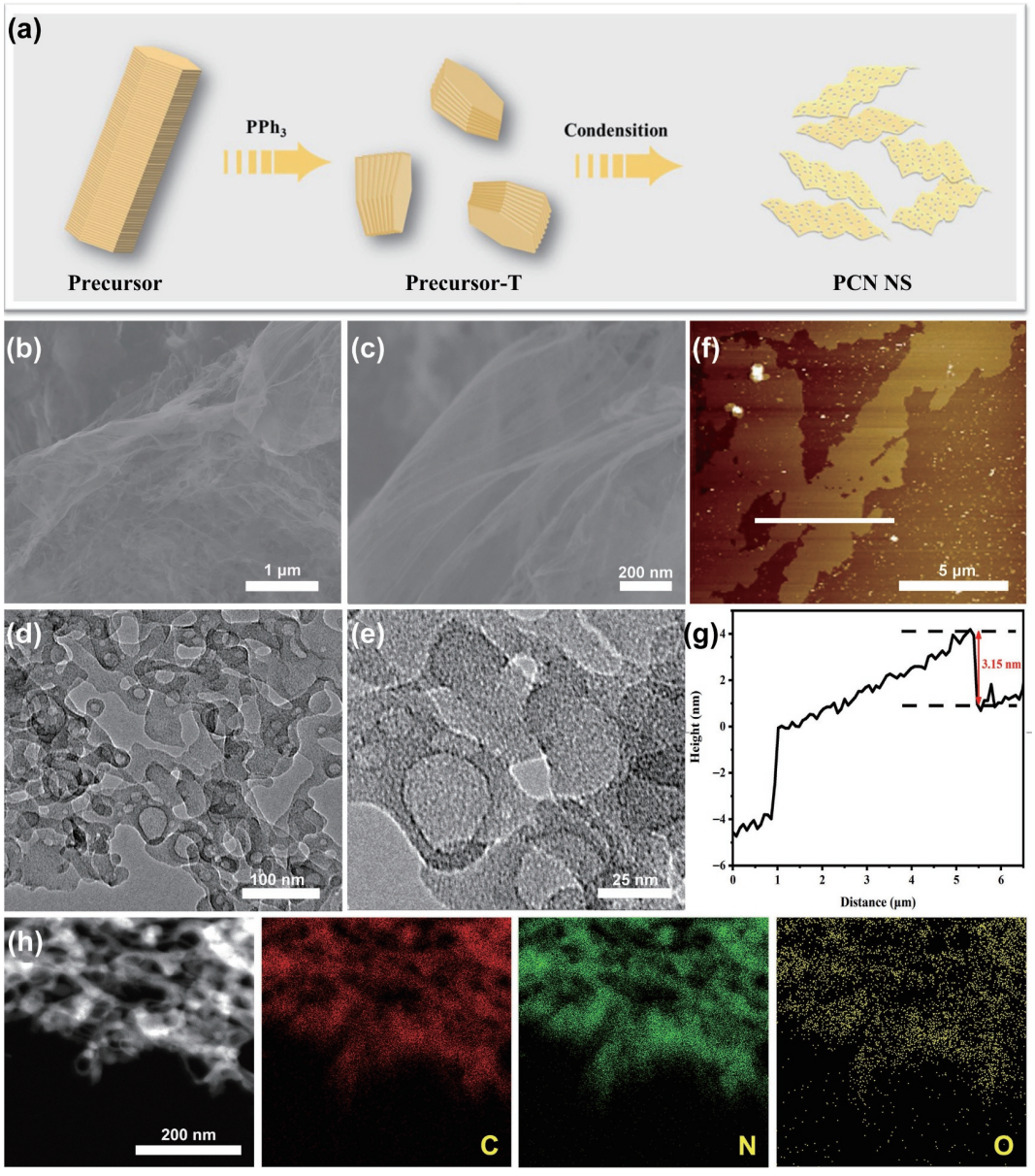

Figure 1 (a) Illustration of the preparation process of PCN NS. (b) SEM image of the PCN NS. (c) Magnified SEM image of the PCN NS. (d) TEM image of the PCN NS. (e) Magnified TEM image of the PCN NS. (f) AFM image and (g) the corresponding height profiles of PCN NS. (h) STEM image and EDX elemental mappings of PCN NS.

precursor-T (Fig. S6(a) in the ESM) within 1 min (Fig. S6(b) in the ESM). The expansion can be promoted by increasing the calcination to 400 or 450 °C (Figs. S6(c) and S6(d) in the ESM). A large number of thin sheets can be formed by the calcination at 500 °C for 1 min (Fig. S6(e) in the ESM). Further increase of the calcination time to 2 h, the sample evolved into an ultrathin 2D porous structure (Fig. S6(f) in the ESM). The results show that the exfoliation of precursor-T is a fast process, which should be ascribed to the release of a large number of gaseous products during the calcination process. The gas can sharply increase the internal pressure of the precursor layers, leading to the rupture of the π–π interaction. At the same time, the gas released during the thermal condensation process can create many pores and finally produce 2D PCN NS.

The transformation of sheet-like precursor-T into g-C_3N_4 is verified by the XRD (Fig. S7 in the ESM). The peaks located at 13.11° and 27.56° are indexed to the (100) and (002) diffraction peaks of g-C_3N_4. Compared with BCN, the (100) peak of PCN NS almost disappears [38]. The disappearance can be attributed to the separation of the repeated conjugated g-C_3N_4 plane, implying the formation of thin sheets. The broad and weak (002) peak also indicates the thin-sheet characterization of the samples. In addition, a broad peak around 22° is attributed to the amorphous phase, implying the low crystallinity of PCN NS [39–41]. The formation of thin sheets can be directly demonstrated by the SEM and TEM. As shown in Figs. 1(b) and 1(c), the SEM image shows the presence of a thin nanosheet in PCN NS samples. There is the presence of the curled margin, like the reduced graphene oxide (rGO), implying the thin-sheet characterization of PCN NS. The formation of pores should be ascribed to the release of gases such as (NH_3, CO_2, H_2O, and NO) during the calcination [42]. The TEM image shows the thin sheets with the plentiful pores having the sizes of 10–50 nm (Figs. 1(d) and 1(e)). The AFM image shows the thickness of the sheets at about 3 nm (Figs. 1(f) and 1(g)). All above tests imply the formation of porous thin sheets based on our "vacuum-assisted expansion" method. Both porous and 2D structures are favorable to increase the surface area. As shown in Fig. S8 in the ESM, the N_2 adsorption–desorption isotherm shows a typical four-type curve and a typical H_3-type hysteresis loop, indicating the porous structure of PCN NS. The specific surface area of PCN NS is about 168.8 $m^2 \cdot g^{-1}$, which is about 36 times of BCN (4.6 $m^2 \cdot g^{-1}$).

The large specific area and porous structure are favorable for the contact of reactants with the catalysts and the transfer mass, which is largely important for effective catalysis. The scanning transmission electron microscopy (STEM) shows the net-like sheets, and corresponding EDX mapping shows the uniform distribution of C, N, and O elements throughout the whole scan area (Fig. 1(h)).

There is the usual presence of N or C vacancies in the g-C_3N_4. In general, the N vacancies can tune the bandgap, act as trap states for photogenerated electrons, and promote charge transfer and separation efficiency [42] because of the π electrons delocalization of the C_3N_4 network by the distribution of e electrons to the nearest carbon atom [43–46]. We have combined several methods to give the information about N vacancies. As shown in the FTIR, there are lower N–H tensile peak intensities (3,000–3,300 cm^{-1}) in PCN NS than that in the BCN, implying the decrease of the N–H group concentration (nitrogen vacancies) in the former (Fig. 2(a)) [42]. Further, the EPR spectroscopy shows a signal with a g value of 2.003 (Fig. 2(b)), attributing to the unpaired electrons on the carbon atoms of the heptazine ring in the π-bonded materials. The peak intensity for PCN NS is much higher than that of BCN, indicating the introduction of more nitrogen vacancies in the PCN NS than that in BCN. The loss of nitrogen atoms will leave excess electrons, thus increasing the concentration of lone pair electrons.

To further determine the nitrogen vacancy, high resolution N 1s XPS spectrum of the PCN NS was given and analyzed (Fig. 2(c)). The spectrum displays three peaks located at 398.3, 399.4, and 400.9 eV, assigned to C=N–C, $(C)_3$–N, and N–H, respectively. Compared to BCN, all the N 1s peaks of PCN NS shift to higher binding energy, indicating the formation of N vacancies [46]. It is worth noting that the peak area ratio between C=N–C and $(C)_3$–N is significantly reduced from 2.35 for BCN to 1.63 for PCN NS, indicating that the nitrogen vacancies are mainly located at the CN=C site [29]. Furthermore, by comparison with BCN, the C 1s peak of PCN NS (Fig. 2(d)) shifts to low binding energy, indicating more electrons around C in PCN NS. This is due to the electron transfer caused by the absence of N. A new peak centered at 286.1 eV appeared in PCN NS, which further confirmed the loss of lattice nitrogen and the formation of nitrogen vacancies [47]. Moreover, the XPS spectrum of the rod-shaped precursor did not find the characteristic P element peak (Fig. S9 in the ESM), indicating that the phosphorous acid molecules adsorbed on the precursor have been completely removed. No obvious P element peak was found in the rod-shaped precursor after TP intercalation, which indicated that TP peeled off the (100) crystal plane and did not remain in the precursor. This corresponds to the XPS spectrum of PCN NS P 2p.

UV–vis absorption spectroscopy shows that both BCN and PCN NS have absorption in the range of 300–800 nm. Compared with BCN, PCN NS has a significant blue shift, which is caused by the quantum confinement effect of ultra-thin structure. Nevertheless, the PCN NS still showed enhanced visible light absorption spanning the entire visible light region, which is mainly due to the enhancement of the photo-generated carrier $n \rightarrow \pi^*$ transition (Fig. S10(a) in the ESM) [48]. Based on the UV–vis spectrum, the band gap of BCN and PCN NS is about 2.66 and 2.76 eV (Fig. S10(b) in the ESM). In addition, we analyzed Mott–Schottky at different frequencies of 1.0k, 1.2k, and 1.4k Hz to determine its electronic band structure (Figs. S11(a) and S11(b) in the ESM). The positive slopes of BCN and PCN NS come from typical n-type characteristic semiconductors. In the Mott–Schottky diagram, the flat band potentials of BCN and PCN NS are −1.10 and −1.02 V (relative to Ag/AgCl), respectively. It is generally believed that the conduction band (CB) potential in n-type semiconductors is approximately equal to the flat band potential, so the CB edges of BCN and PCN NS are −1.10 and −1.02 eV, respectively. The band structure diagram of BCN and PCN NS (Fig. S12 in the ESM) can be drawn by combining the UV–vis spectrum (Fig. S10 in the ESM). The CB of PCN NS

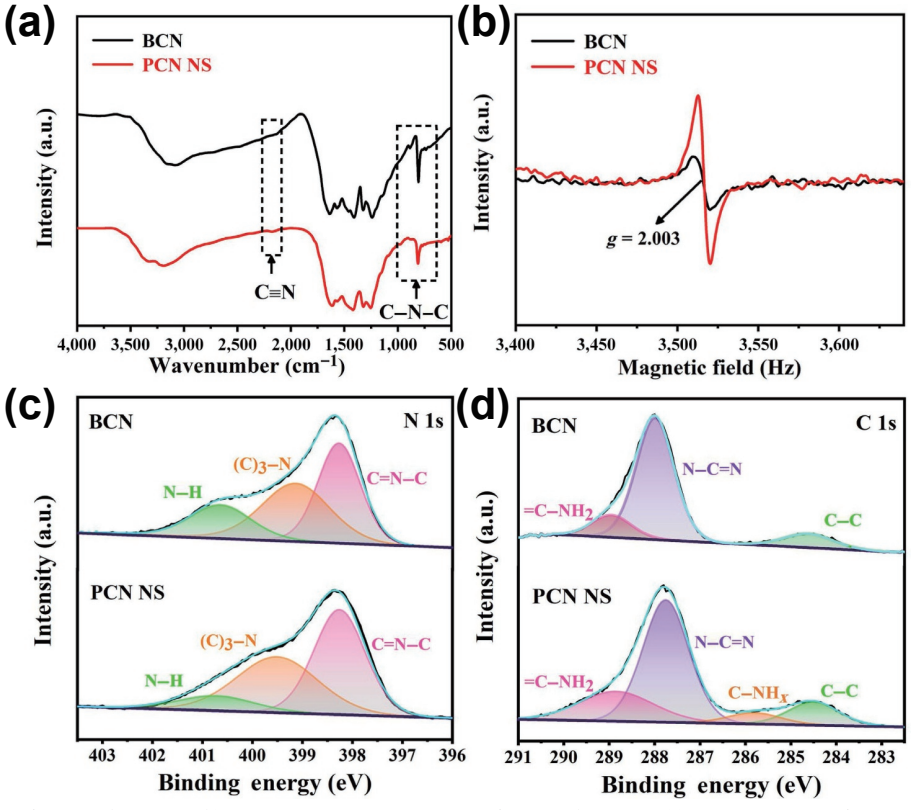

Figure 2 (a) FTIR spectra of BCN and PCN NS. (b) Room-temperature EPR spectra of BCN and PCN NS. (c) N 1s XPS spectra of BCN and PCN NS. (d) C 1s XPS spectra of BCN and PCN NS.

moves down by 0.08 eV in comparison with BCN, which is mainly due to the formation of defect states caused by nitrogen vacancies [47]. Although the CB potential of PCN NS decreases, it is still more negative than the reduction potential of H^+/H_2. The analysis of band structure shows that the band edge of PCN NS satisfies the thermodynamic requirements of PHE from water.

The combined characterizations of the 2D structure, plentiful pores and rich N vacancies are favorable for photocatalysis. The steady-state PL spectrum of the photocatalyst is shown in Fig. S13 in the ESM. The main emission peak of the PCN NS and BCN appears at 460 and 470 nm. A blue shift of the peaks for PCN NS in the comparison with that of BCN is consistent with the change of the band gap and the thin-sheet characteristics of PCN NS. In addition, compared with that of BCN, the PL intensity of PCN NS is significantly reduced, indicating the lower electron–hole recombination rate of PCN NS than that of BCN.

The primary tests show that, in the presence of 1 wt.% Pt, the hydrogen production activity over PCN NS is 42 times (AM1.5) and 16 times (cut 400) of that over BCN. The hydrogen production activity can reach 108.0 $\mu mol \cdot h^{-1} \cdot g^{-1}$ in the absence of a cocatalyst under simulated sunlight (Fig. S14 in the ESM). As known, the non-Pt PHE is important due to the high price and low reserve of Pt metals. Among many co-catalysts developed, the MoS_2 are of most promising and frequently studied co-catalysts because the free energy of the H adsorption on edge sites of transition metal dichalcogenides (TMDs) is close to that on Pt [49]. It is desirable to load the few-layered and well-dispersed MoS_2 on g-C_3N_4 for exposure to the more active sites [50]. Our previous studies show the loading of the small-size and well-dispersed MoP and Mo_2N on 2D graphene by using polyoxometalate (POM) clusters as a precursor [51]. So, we have adopted a method based on the coupling of g-C_3N_4 and PMo_{12} clusters (Mo source) by PEI for the growth of few-layered and well-dispersed MoS_2 on g-C_3N_4. The PEI has processed rich positively charged amines that can combine with negatively charged colloids or ions. The zeta potential value of PEI-PCN NS was measured to be +38.8 mV when dispersed in DI water, and it is −17.6 mV for PCN NS (Fig. S2 in the ESM). Therefore, the PEI can combine with the PCN NS to form a positively charged PEI-PCN NS. In DI water, phosphomolybdic acid can ionize into discrete negatively charged anions $[PMo_{12}O_{40}]^{3-}$. The anions can combine with the amines in PEI-PCN NS to obtain PMo_{12}/PCN NS complexes. Through the sulfurization, the MoS_2/PCN NS can be formed (Fig. 3(a)). The coupling action of PEI can inhibit the over-growth and server aggregation of the particles, to form the uniform and few-layered MoS_2. As shown in Fig. S15(a) in the ESM, the activity test of MoS_2/PCN NS (P) synthesized with different PMo_{12} loading capacity was carried out. When the PMo_{12} loading capacity was 20%, the photocatalytic hydrogen production capacity was the best. TG test showed that the true content of the

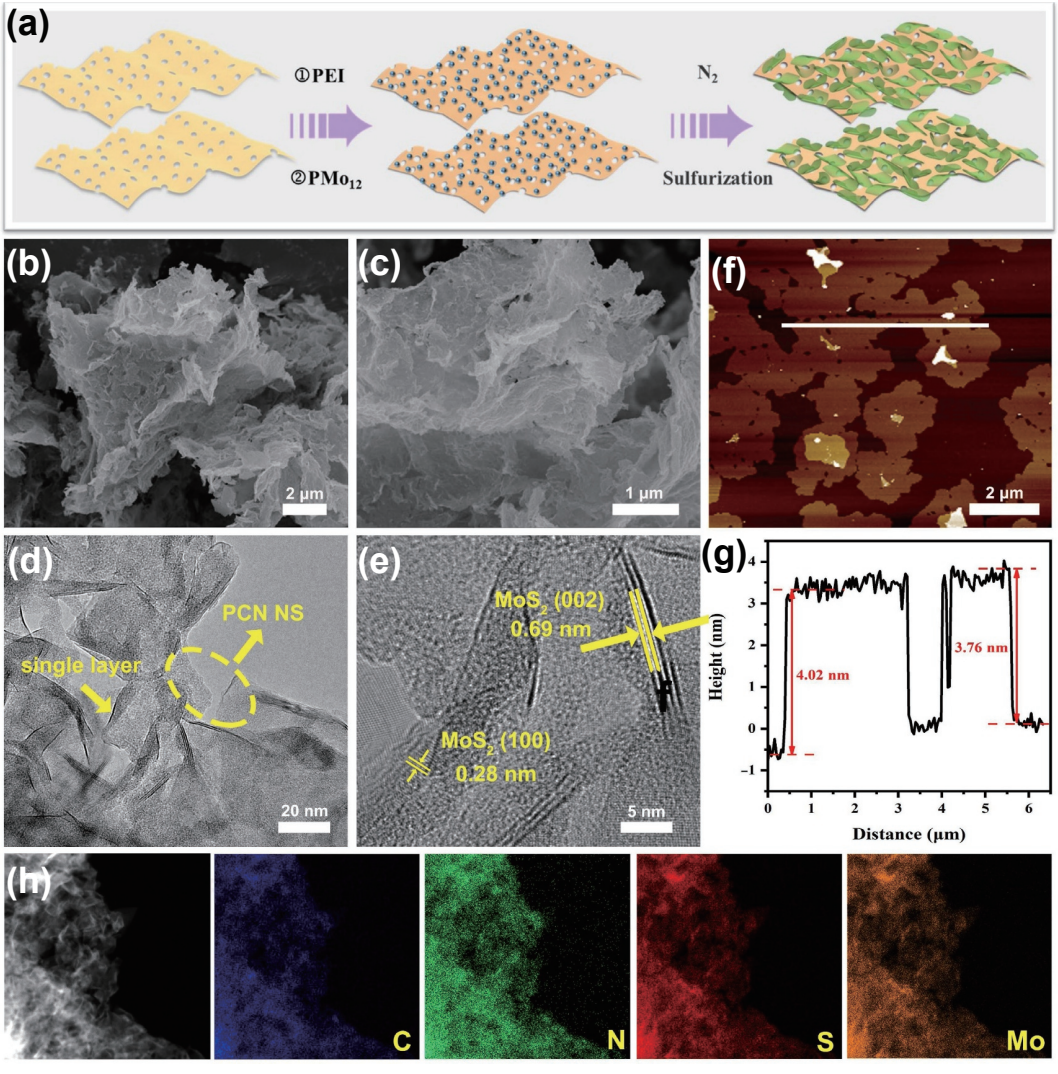

Figure 3 (a) Illustration of the preparation process of MoS_2/PCN NS (P). (b) SEM image of the MoS_2/PCN NS (P). (c) Magnified SEM image of the MoS_2/PCN NS (P). (d) TEM image of the MoS_2/PCN NS (P). (e) Magnified TEM image of the MoS_2/PCN NS (P). (f) AFM image of MoS_2/PCN NS (P). (g) the corresponding height profiles of MoS_2/PCN NS (P). (h) STEM image and EDX elemental mappings of MoS_2/PCN NS (P).

best active catalyst MoS_2 was about 4% of MoS_2/PCNS (Fig. S15(b) in the ESM).

The XRD pattern (Fig. S16 in the ESM) of MoS_2/PCN NS (P) shows three peaks at 27.5°, 33.2°, and 58.8° respectively, which can be attributed to the (002) interlayer stacking peak of PCN NS and (100) and (110) peak of MoS_2 [52]. The peaks (located at ≈ 13°) regarding as the (002) peak of MoS_2 cannot be seen, which implies the few-layered/single-layered characterization of MoS_2. The SEM image obviously shows the ultra-thin and curled 2D thin-sheet structure, like the original PCN NS. The test implies the formation of thin MoS_2 sheets on PCN NS (Figs. 3(b) and 3(c)). The TEM image shows the uniform growth of MoS_2 on PCN NS (Fig. 3(d)). The enlarged TEM image (Fig. 3(e)) shows the fringes with a lattice spacing of 0.28 and 0.69 nm, corresponding to the (100) and (002) crystal planes of MoS_2 [53]. The fewer-layered MoS_2 benefits from to exposure more active sites. Also, we can observe the intimate contact of MoS_2 and PCN NS, being favorable for the transfer of electrons. For MoS_2/PCN NS (I) from the immersion method, the TEM image shows the aggregated, thick MoS_2 sheets on the PCN NS (Fig. S17(a) in the ESM). The MoS_2/PCN NS (P) has a size of about 15 nm (Fig. 3(e)), while MoS_2/PCN NS (I) composite prepared without PEI has a size of about 25 nm (Fig. S17(b) in the ESM). By calculating the active site at the edge of MoS_2, MoS_2/PCN NS (P) composites exposed to active sites at the edge of 8.3%, much higher than MoS_2/PCN NS (I) of 4% [54]. This further proves the advantage of few-layered MoS_2 over multi-layered MoS_2. The analysis demonstrated that the PEI coupling method is conducive to giving MoS_2 with the exposure of more active sites at the edge. The AFM image shows the thin-sheet MoS_2/PCN NS (P) with a thickness of about 4 nm (Figs. 3(f) and 3(g)). As shown in Fig. 3(h), STEM clearly shows that C, N, S, and Mo elements were uniformly distributed throughout the NS. The sheet is slightly thicker than that of PCN NS, which further verifying the growth of thin MoS_2 on PCN NS (P). The characterization makes the high BET specific areas of MoS_2/PCN NS (P) (192 $m^2 \cdot g^{-1}$) (Fig. S8 in the ESM).

In order to further analyze the chemical composition and valence state, we performed XPS measurements. Figures 2(d) and 4(a) show the high-resolution C 1s XPS spectra of PCN NS and MoS_2/PCN NS (P). There are four peaks at 284.6, 286.1, 288, and 289 eV in the MoS_2/PCN NS (P) catalyst, which correspond to the C in C–C, C–NH_x, N–C=N, and =C–NH_2. Compared with that in PCN NS, the C 1s peaks in MoS_2/PCN NS (P) show a positive shift of 0.4 eV. Figure 4(b) shows the high-resolution N 1s XPS spectra of MoS_2/PCN NS (P). The peaks located at 398.6, 399.7, and 401.0 eV are attributed to C=N–C, $(C)_3$–N, and N–H, respectively. Compared with that in PCN NS (Fig. 2(c)), the N 1s peaks show a positive shift of 0.3 eV. Figure 4(c) shows the high-resolution XPS spectrum of Mo 3d. The binding energies located at 229.3 ($3d_{5/2}$) and 232.4 eV ($3d_{3/2}$) can be indexed to Mo^{4+} in MoS_2. The two peaks at 232.6 and 235.4 eV are attributed to $3d_{5/2}$ and $3d_{3/2}$ of Mo^{6+} in MoO_3, and the other two peaks at 230.5 and 233.8 eV are attributed to $3d_{5/2}$ and $3d_{3/2}$ of Mo^{5+}. The emergency of Mo^{6+} and Mo^{5+} should be due to the slight oxidation of Mo^{4+} in MoS_2 [55]. Compared with single-layer and few-layer MoS_2 [56, 57], a negative shift of 0.3 eV can be seen for the Mo 3d peaks of Mo^{4+}. The negative shift indicates the increase of the number of the electrons around Mo, which may be ascribed to the electrons moving to molybdenum sulfide. Figure 4(d) shows the S 2p high-resolution XPS spectrum of MoS_2/PCN NS (P). The S 2p binding energy is located at 162.1 ($2p_{3/2}$) and 163.2 eV ($2p_{1/2}$). Compared with single MoS_2, a negative shift of 0.4 eV for S 2p can be seen. This result proves that the number of electrons around molybdenum sulfide increases, which is attributed to the effective electron transfer between PCN NS (P) and MoS_2. The two peaks appearing at 164.1 and 165.2 eV are attributed to the elemental sulfur on the catalyst surface [54]. The results further confirmed the formation of MoS_2/PCN NS (P) and the transfer of electrons

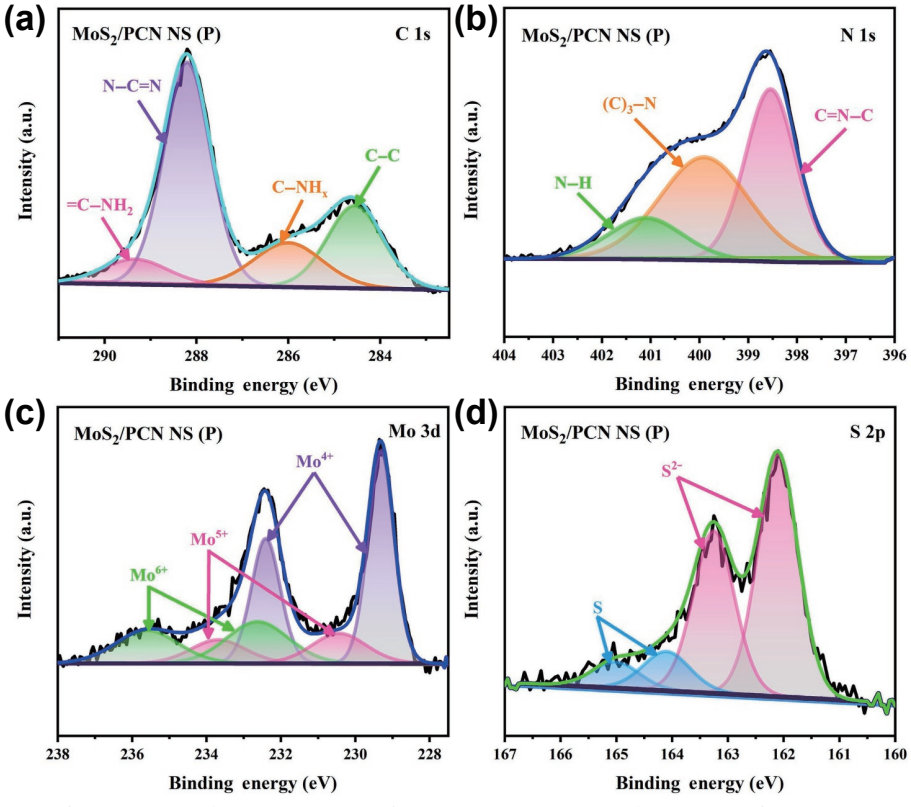

Figure 4 (a) C 1s XPS spectra of MoS_2/PCN NS. (b) N 1s XPS spectra of MoS_2/PCN NS (P). (c) Mo 3d XPS spectra of MoS_2/PCN NS (P). (d) S 2p XPS spectra of MoS_2/PCN NS (P).

from PCN NS to MoS_2, which is largely helpful to improve photocatalytic performance. The optical properties of the sample were detected by UV–visible light absorption spectroscopy (Fig. S18(a) in the ESM). After loading MoS_2, the light absorption in the range of 450–800 nm was significantly enhanced, which may be due to the enhanced light absorption caused by the dark-colored MoS_2 sheet. The results show that the MoS_2/PCN NS (P) sample has a stronger utilization of incident photons and a wider light absorption range, being consistent with a narrowing band gap (Fig. S18(b) in the ESM). This is conducive to improving the performance of photocatalytic hydrogen production.

3.2 Photocatalytic H_2 evolution performance

Above characterizations imply the potential of the catalysts for solar photocatalysis. The photocatalytic activity of MoS_2/PCN NS (P) for hydrogen evolution was investigated by using methanol as a sacrifice electron donor and under simulated sunlight irradiation. As shown in Fig. 5(a), the average hydrogen evolution rate of MoS_2/PCN NS (P) reached 4,270.8 μmol·h^{-1}·g^{-1}, which was 39 times higher than that of PCN NS (108.0 μmol·h^{-1}·g^{-1}) and 8 times higher than that of MoS_2/BCN (P) (533.7 μmol·h^{-1}·g^{-1}). This result proves that MoS_2 is an effective cocatalyst for hydrogen evolution. Also, the comparison emphasizes the advantages of 2D PNC NS over BCN for PHE. In addition, the PHE activity of MoS_2/PCN NS (P) was much higher than that of MoS_2/PCN NS (I) (463.7 μmol·h^{-1}·g^{-1}). The improvement can be relative to the few-layered and high-dispersed characterization of MoS_2 in MoS_2/PCN NS (P) benefited from the PEI-coupling method. Moreover, as shown in Fig. 5(b), after 5 cycles of testing within a 20-h photocatalytic operation, the H_2 yield did not decrease significantly, indicating that MoS_2/PCN NS (P) has high stability under the applied reaction conditions. To better understand the origin of good photocatalytic performance, the photoelectrochemical properties of MoS_2/BCN (P) and MoS_2/PCN NS (P) photoanodes were studied. The separation efficiency of electron–hole pairs is a key parameter that determines the solar absorption and conversion capabilities, which was evaluated by LSV. Obviously, the LSV shows higher photocurrent density for MoS_2/PCN NS (P) under AM1.5 than MoS_2/BCN (P) (Fig. S19 in the ESM), illustrating the more efficient separation of photogenerated charges. Figure 5(c) shows the room temperature PL spectrum. According to the normal PL results, the main emission wavelength of all samples (excited at 375 nm) is located at ≈ 450 nm, which can be attributed to the band gap luminescence of g-C_3N_4. It is worth noting that, compared with that of MoS_2/BCN (P), the PL spectrum of MoS_2/PCN NS (P) shows a blue shift. This shift is attributed to the

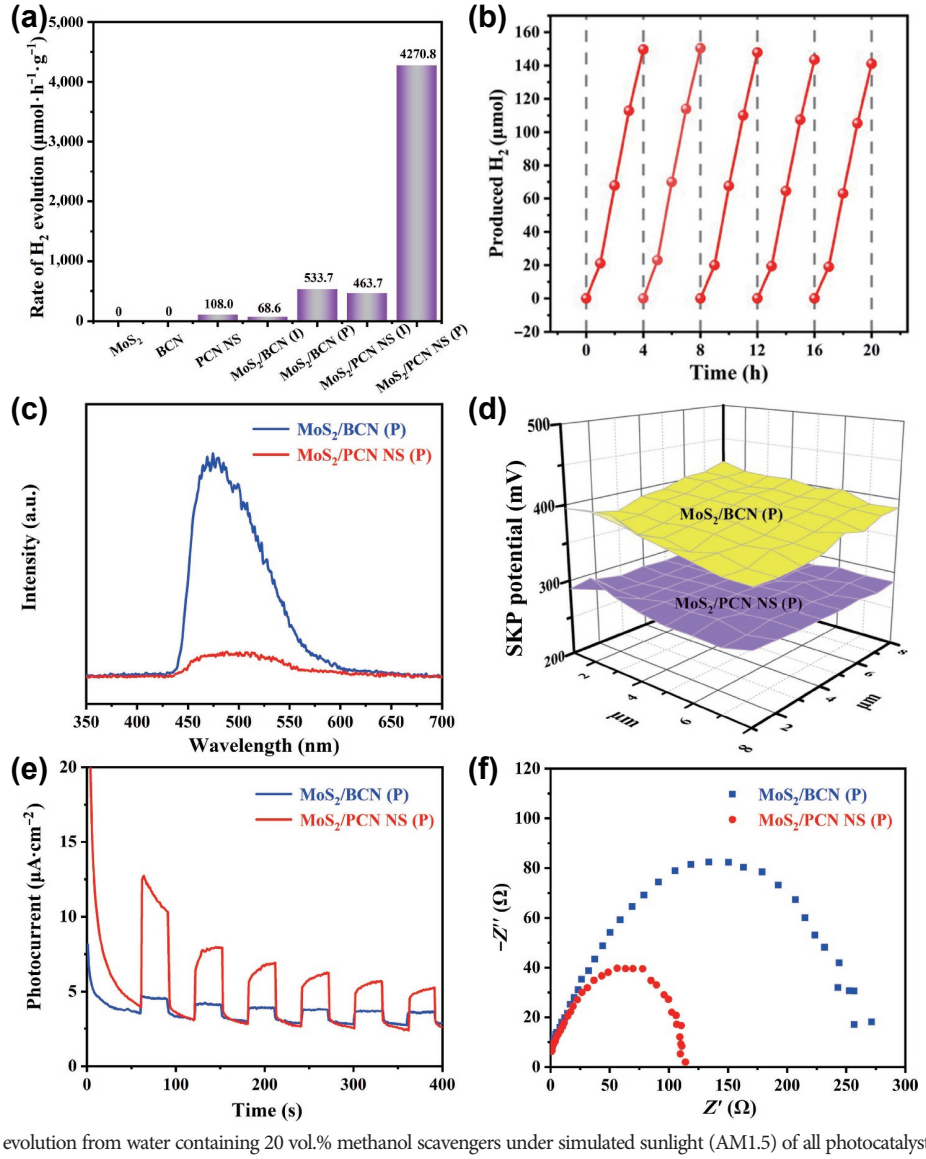

Figure 5 (a) Hydrogen evolution from water containing 20 vol.% methanol scavengers under simulated sunlight (AM1.5) of all photocatalysts. (b) Time course of H_2 evolution for under simulated sunlight. (c) Steady state PL spectra of MoS_2/BCN (P) and MoS_2/PCN NS (P). (d) SKP maps of MoS_2/BCN (P) and MoS_2/PCN NS (P). (e) The transient photocurrent responses of MoS_2/BCN (P) and MoS_2/PCN NS (P). (f) EIS Nyquist plots of MoS_2/BCN (P) and MoS_2/PCN NS (P) electrodes.

wideband gap characteristics of ultra-thin structures [21], which can also be confirmed by the UV–vis diffuse reflectance spectra (Fig. S10(a) in the ESM). The scanning Kelvin probe (SKP) is sensitive to discern subtle molecular interactions through vibrating electromagnetic and acoustic fields, which shows a relatively flat potential change in terms of work function (WF). As shown in Fig. 5(d), the WF of MoS_2/PCN NS (P) (5.64 eV) is lower than that of MoS_2/BCN (P) (5.72 eV), which ensures easier escape of electrons from MoS_2/PCN NS (P) catalysts to H* for PHE [58]. According to SKP results, the approximate Fermi level of MoS_2/PCN NS (P) is higher than that of MoS_2/BCN (P), which changes the built-in electric field and surface band bending. So, the ultrathin structure can accelerate the transfer of photogenerated carriers to the cocatalyst, thus greatly reducing the electron–hole recombination and improving the photocatalytic performance. To gain insight into the charge transport efficiency, the transient photocurrents of MoS_2/BCN (P) and MoS_2/PCN NS (P) electrodes were measured. As shown in Fig. 5(e), both electrodes exhibited fast and uniform photocurrent responses under intermittently visible light irradiation. Compared with MoS_2/BCN (P), the MoS_2/PCN NS (P) photoelectrode shows a much higher photocurrent response. The result indicates that the transfer and separation of charge carrier later were greatly enhanced, being consistence with the PL analysis. A similar trend was also observed in EIS measurement (Fig. 5(f)). As shown, the MoS_2/PCN NS (P) shows the smallest arc radius in all samples, indicating its low resistance for fast interfacial charge carrier transfer. In summary, the unique 2D porous structure MoS_2/PCN NS (P), large specific surface area, and intimate contact of MoS_2 with PCN NS can contribute to the good charge separation ability that shortens the migration distance of photo-generated carriers, thus giving improved the photocatalytic activity.

3.3 Band structure and charge transfer

The band structure of MoS_2/PCN NS (P) was studied to give some insight into the photocatalytic process. The CB positions of PCN NS and MoS_2 were measured by Mott–Schottky plots at frequencies of 1.0k, 1.2k, and 1.4k Hz. Both PCN NS and MoS_2 exhibit a positive slope, which are consistent with the character of a typical n-type semiconductors (Fig. S11(b) in the ESM and Fig. 6(a)). The flat band potentials of PCN NS and MoS_2 are −1.02 and −0.84 V (relative to Ag/AgCl), respectively. It is generally believed that the CB potential in n-type semiconductors is approximately equal to the flat band potential, so the CB edges of PCN NS and MoS_2 are −1.02 and −0.84 eV, respectively. In addition, based on the UV–vis spectrum, the band gap of PCN NS and MoS_2 is about 2.77 and 1.80 eV (Fig. S10(b) in the ESM and Fig. 6(b)).

So, the potentials of the valence bands of PCN NS and MoS_2 are calculated to be 1.75 and 0.96 eV by a combined analysis of bandgaps and CB edges. The results indicate the formation of a Type I heterojunction between PCN NS and MoS_2 (Fig. 6(c)). Based on the above analyses, we proposed a mechanism of charge transfer promoted by the synergistic interaction between MoS_2 and PCN NS. As shown in Fig. 6(d), when the MoS_2/PCN NS (P) is illuminated by light, the electrons and holes are generated in PCN NS. In MoS_2/PCN NS (P), the MoS_2 can act as an electron acceptor. The electrons at the CB of PCN NS are rapidly transferred to the CB of the MoS_2, which can subsequently participate in the evolution of H_2, and the holes in the valence band (VB) of PCN NS can be transferred to the VB of MoS_2 and react with methanol. The excellent photocatalytic hydrogen production activity of MoS_2/PCN NS (P) originates from several aspects. (1) The ultra-thin structure of PCN NS shortens the electron–hole transfer distance; (2) the pore structure of PCN NS is conducive to the mass transfer process and accelerates the redox

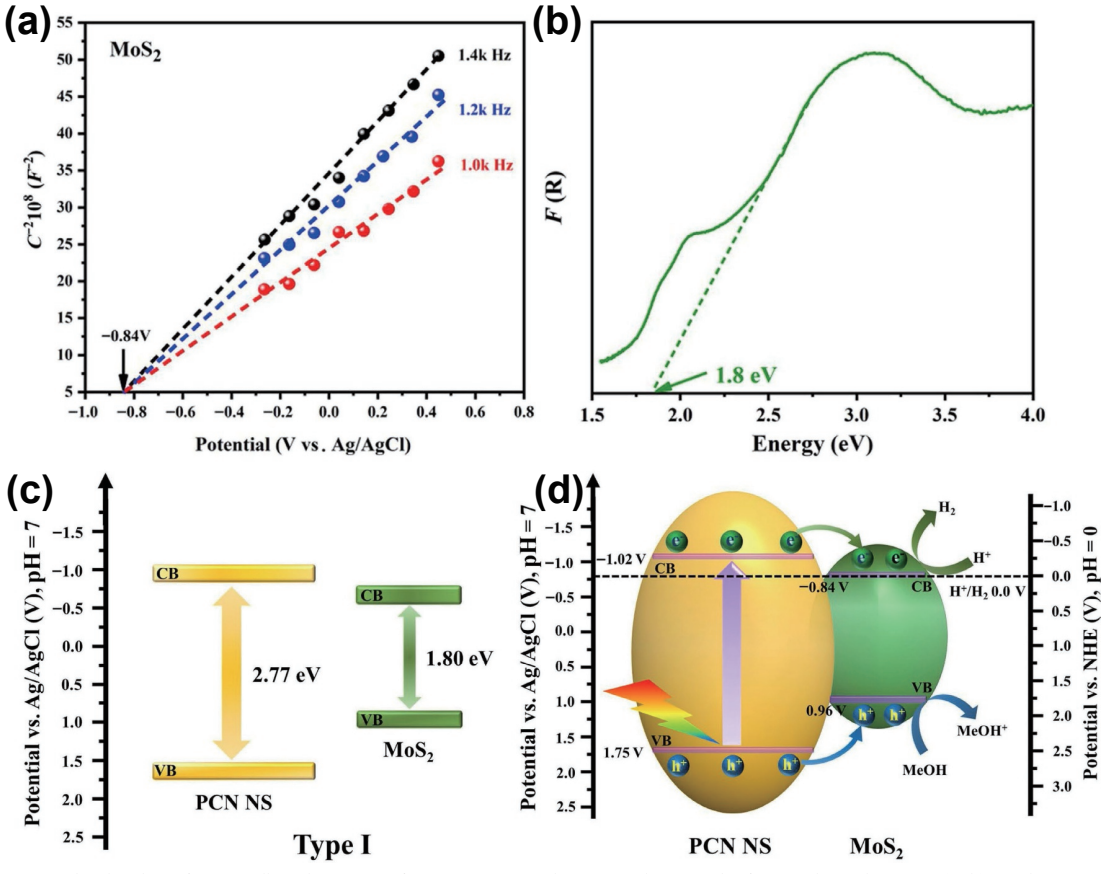

Figure 6 (a) Mott–Schottky plots of MoS_2 collected at various frequencies versus the saturated Ag/AgCl reference electrode (pH = 7). (b) Band gap energies of MoS_2. (c) Electronic band structure of MoS_2 and PCN NS. (d) Scheme illustration of the charge transfer behavior of MoS_2/PCN NS (P) under simulated irradiation

reaction, and the ultra-thin porous structure can increase the specific surface area, which is conducive to the better growth of the cocatalyst; (3) the introduction of nitrogen defects in PCN NS facilitates the separation and transfer of charge carriers in π conjugate plane, inhibiting the recombination of electron–hole pairs for effectively improving the PHE rate; (4) benefiting from the intimate contact of MoS_2 and PCN NS, the photogenerated electrons in the CB of PCN NS can be easily transferred to few-layer MoS_2, then reducing water to form hydrogen. In addition, the few-layer MoS_2 can provide plenty of the unsaturated active S atoms that can bond to H^+ in the solution. Thus, the few-layer MoS_2 in this system can not only guide and accelerate charge transfer but also provide a large number of active sites at the edge sites and base planes of hydrogen production. Under simulated light irradiation, PCN NS was excited, and the electrons and holes were then generated.

4 Conclusions

In summary, we have demonstrated a new method for the synthesis of 2D PCN thin sheets, which are characterized by the large accessible surface, plentiful pores, and N defects. The PCN NS can combine with a few-layered MoS_2 by a PEI coupling method. The few-layered MoS_2 has abundant edge active sites, and its intimate combination with porous PCN NS is favorable for the faster transfer and effective separation of the electrons, being responsible for the enhanced photocatalytic activity. The tests showed the excellent photocatalytic activity of the MoS_2/PCN NS (P) with the high hydrogen production activity of 4,270.8 $\mu mol \cdot h^{-1} \cdot g^{-1}$ under the simulated sunlight condition, which was 7.9 times of the corresponding MoS_2/BCN(P) and 12.7 times of the 1 wt.% Pt/BCN. This work not only provides a new strategy toward 2D PCN thin sheets, but also shows the advantage of constructing intimate 2D–2D MoS_2/g-C_3N_4 heterojunction for efficient catalysis.

Acknowledgements

This work was financially supported by the National Key R&D Program of China (No. 2018YFB1502401), the National Natural Science Foundation of China (Nos. 91961111, U20A20250, and 21901064), the Natural Science Foundation of Heilongjiang Province (No. ZD2021B003), the University Nursing Program for Young Scholars with Creative Talents in Heilongjiang Province (No. UNPYSCT-2020004), the Basic Research Fund of Heilongjiang University in Heilongjiang Province (No. 2021-KYYWF-0039), and Open Project of Key Laboratory of Polyoxometalate and Reticular Material Chemistry of Ministry of Education.

Electronic Supplementary Material: Supplementary material (structural characterization of precursors and catalytic performance of reference samples) is available in the online version of this article at https://doi.org/10.1007/s12274-022-4900-7.

References

[1] Ong, W. J.; Tan, L. L.; Ng, Y. H.; Yong, S. T.; Chai, S. P. Graphitic carbon nitride (g-C_3N_4)-based photocatalysts for artificial photosynthesis and environmental remediation: Are we a step closer to achieving sustainability? *Chem. Rev.* **2016**, *116*, 7159–7329.

[2] Zhou, Z. X.; Zhang, Y. Y.; Shen, Y. F.; Liu, S. Q.; Zhang, Y. J. Molecular engineering of polymeric carbon nitride: Advancing applications from photocatalysis to biosensing and more. *Chem. Soc. Rev.* **2018**, *47*, 2298–2321.

[3] Wang, X. C.; Maeda, K.; Thomas, A.; Takanabe, K.; Xin, G.; Carlsson, J. M.; Domen, K.; Antonietti, M. A metal-free polymeric photocatalyst for hydrogen production from water under visible light. *Nat. Mater.* **2009**, *8*, 76–80.

[4] Zheng, Y.; Lin, L. H.; Wang, B.; Wang, X. C. Graphitic carbon nitride polymers toward sustainable photoredox catalysis. *Angew. Chem., Int. Ed.* **2015**, *54*, 12868–12884.

[5] Hao, Q.; Jia, G. H.; Wei, W.; Vinu, A.; Wang, Y.; Arandiyan, H.; Ni, B. J. Graphitic carbon nitride with different dimensionalities for energy and environmental applications. *Nano Res.* **2020**, *13*, 18–37.

[6] Nasir, M. S.; Yang, G. R.; Ayub, I.; Wang, S. L.; Wang, L.; Wang, X. J.; Yan, W.; Peng, S. J.; Ramakarishna, S. Recent development in graphitic carbon nitride based photocatalysis for hydrogen generation. *Appl. Catal. B Environ.* **2019**, *257*, 117855.

[7] Wang, Y.; Phua, S. Z. F.; Dong, G.; Liu, X. Q.; He, B.; Zhai, Q. L.; Li, Y. C.; Zheng, C. C.; Quan, H. P.; Li, Z. et al. Structure tuning of polymeric carbon nitride for solar energy conversion: From nano to molecular scale. *Chem* **2019**, *5*, 2775–2813.

[8] Liu, J.; Wang, H. Q.; Antonietti, M. Graphitic carbon nitride "reloaded": Emerging applications beyond (photo)catalysis. *Chem. Soc. Rev.* **2016**, *45*, 2308–2326.

[9] Chen, F.; Ma, Z. Y.; Ye, L. Q.; Ma, T. Y.; Zhang, T. R.; Zhang, Y. H.; Huang, H. W. Macroscopic spontaneous polarization and surface oxygen vacancies collaboratively boosting CO_2 photoreduction on $BiOIO_3$ single crystals. *Adv. Mater.* **2020**, *32*, 1908350.

[10] Liu, L. Z.; Huang, H. W.; Chen, Z. S.; Yu, H. J.; Wang, K. Y.; Huang, J. D.; Yu, H.; Zhang, Y. H. Synergistic polarization engineering on bulk and surface for boosting CO_2 photoreduction. *Angew. Chem., Int. Ed.* **2021**, *60*, 18303–18308.

[11] Wang, S. B.; Han, X.; Zhang, Y. H.; Tian, N.; Ma, T. Y.; Huang, H. W. Inside-and-out semiconductor engineering for CO_2 photoreduction: From recent advances to new trends. *Small Struct.* **2021**, *2*, 2000061.

[12] Zhou, L.; Zhuang, Z. C.; Zhao, H. H.; Lin, M. T.; Zhao, D. Y.; Mai, L. Q. Intricate hollow structures: Controlled synthesis and applications in energy storage and conversion. *Adv. Mater.* **2017**, *29*, 1602914.

[13] Xiao, M.; Wang, Z. L.; Lyu, M.; Luo, B.; Wang, S. C.; Liu, G.; Cheng, H. M.; Wang, L. Z. Hollow nanostructures for photocatalysis: Advantages and challenges. *Adv. Mater.* **2019**, *31*, 1801369.

[14] Zhang, X. D; Wang, H. X.; Wang, H.; Zhang, Q.; Xie, J. F.; Tian, Y. P.; Wang, J.; Xie, Y. Single-layered graphitic-C_3N_4 quantum dots for two-photon fluorescence imaging of cellular nucleus. *Adv. Mater.* **2014**, *26*, 4438–4443.

[15] Zhao, D. M.; Wang, Y. Q.; Dong, C. L.; Huang, Y. C.; Chen, J.; Xue, F.; Shen, S. H.; Guo, L. J. Boron-doped nitrogen-deficient carbon nitride-based Z-scheme heterostructures for photocatalytic overall water splitting. *Nat. Energy* **2021**, *6*, 388–397.

[16] Zhang, J. S.; Chen, Y.; Wang, X. C. Two-dimensional covalent carbon nitride nanosheets: Synthesis, functionalization, and applications. *Energy Environ. Sci.* **2015**, *8*, 3092–3108.

[17] Hou, Y.; Wen, Z. H.; Cui, S. M.; Guo, X. R.; Chen, J. H. Constructing 2D porous graphitic C_3N_4 nanosheets/nitrogen-doped graphene/layered MoS_2 ternary nanojunction with enhanced photoelectrochemical activity. *Adv. Mater.* **2013**, *25*, 6291–6297.

[18] Wang, Y. H.; Liu, L. Z.; Ma, T. Y.; Zhang, Y. H.; Huang, H. W. 2D graphitic carbon nitride for energy conversion and storage. *Adv. Funct. Mater.* **2021**, *31*, 2102540.

[19] Gupta, U.; Rao, C. N. R. Hydrogen generation by water splitting using MoS_2 and other transition metal dichalcogenides. *Nano Energy* **2017**, *41*, 49–65.

[20] Gong, S. Q.; Jiang, Z. J.; Shi, P. H.; Fan, J. C.; Xu, Q. J.; Min, Y. L. Noble-metal-free heterostructure for efficient hydrogen evolution in visible region: Molybdenum nitride/ultrathin graphitic carbon nitride. *Appl. Catal. B Environ.* **2018**, *238*, 318–327.

[21] Liu, Y. Z.; Zhang, H. Y.; Ke, J.; Zhang, J. Q.; Tian, W. J.; Xu, X. Y.; Duan, X. G.; Sun, H. Q.; Tade, M. O.; Wang, S. B. 0D (MoS_2)/2D (g-

C_3N_4) heterojunctions in Z-scheme for enhanced photocatalytic and electrochemical hydrogen evolution. *Appl. Catal. B Environ.* **2018**, *228*, 64–74.

[22] Yuan, Y. J.; Shen, Z. K.; Wu, S. T.; Su, Y. B.; Pei, L.; Ji, Z. G.; Ding, M. Y.; Bai, W. F.; Chen, Y. F.; Yu, Z. T. et al. Liquid exfoliation of g-C_3N_4 nanosheets to construct 2D–2D MoS_2/g-C_3N_4 photocatalyst for enhanced photocatalytic H_2 production activity. *Appl. Catal. B Environ.* **2019**, *246*, 120–128.

[23] Bian, H.; Ji, Y. J.; Yan, J. Q.; Li, P.; Li, L.; Li, Y. Y.; Liu, S. Z. *In situ* synthesis of few-layered g-C_3N_4 with vertically aligned MoS_2 loading for boosting solar-to-hydrogen generation. *Small* **2018**, *14*, 1703003.

[24] Sun, Y. Y.; Chen, Z. Z.; Gong, H. P.; Li, X. Q.; Gao, Z. F.; Xu, S. C.; Han, X. D.; Han, B.; Meng, X. W.; Zhang, J. Continuous "snowing" thermotherapeutic graphene. *Adv. Mater.* **2020**, *32*, 2002024.

[25] Shi, L.; Chang, K.; Zhang, H. B.; Hai, X.; Yang, L. Q.; Wang, T.; Ye, J. H. Drastic enhancement of photocatalytic activities over phosphoric acid protonated porous g-C_3N_4 nanosheets under visible light. *Small* **2016**, *12*, 4431–4439.

[26] Ou, H. H.; Lin, L. H.; Zheng, Y.; Yang, P. J.; Fang, Y. X.; Wang, X. C. Tri-s-triazine-based crystalline carbon nitride nanosheets for an improved hydrogen evolution. *Adv. Mater.* **2017**, *29*, 1700008.

[27] Zhang, G.; Ji, Q. H.; Wu, Z.; Wang, G. C.; Liu, H. J.; Qu, J. H.; Li, J. H. Facile "spot-heating" synthesis of carbon dots/carbon nitride for solar hydrogen evolution synchronously with contaminant decomposition. *Adv. Funct. Mater.* **2018**, *28*, 1706462.

[28] Tian, S. F.; Chen, S. D.; Ren, X. T.; Cao, R. H.; Hu, H. Y.; Bai, F. Bottom–up fabrication of graphitic carbon nitride nanosheets modified with porphyrin via covalent bonding for photocatalytic H_2 evolution. *Nano Res.* **2019**, *12*, 3109–3115.

[29] Xiao, Y. T.; Tian, G. H.; Li, W.; Xie, Y.; Jiang, B. J.; Tian, C. G.; Zhao, D. Y.; Fu, H. G. Molecule self-assembly synthesis of porous few-layer carbon nitride for highly efficient photoredox catalysis. *J. Am. Chem. Soc.* **2019**, *141*, 2508–2515.

[30] Guo, S. E.; Deng, Z. P.; Li, M. X.; Jiang, B. J.; Tian, C. G.; Pan, Q. J.; Fu, H. G. Phosphorus-doped carbon nitride tubes with a layered micro-nanostructure for enhanced visible-light photocatalytic hydrogen evolution. *Angew. Chem., Int. Ed.* **2016**, *55*, 1830–1834.

[31] Schwinghammer, K.; Tuffy, B.; Mesch, M. B.; Wirnhier, E.; Martineau, C.; Taulelle, F.; Schnick, W.; Senker, J.; Lotsch, B. V. Triazine-based carbon nitrides for visible-light-driven hydrogen evolution. *Angew. Chem., Int. Ed.* **2013**, *52*, 2435–2439.

[32] Ando, N.; Yamada, T.; Narita, H.; Oehlmann, N. N.; Wagner, M.; Yamaguchi, S. Boron-doped polycyclic π-electron systems with an antiaromatic borole substructure that forms photoresponsive B–P lewis adducts. *J. Am. Chem. Soc.* **2021**, *143*, 9944–9951.

[33] Yan, H. J.; Tian, C. G.; Wang, L.; Wu, A. P.; Meng, M. C.; Zhao, L.; Fu, H. G. Phosphorus-modified tungsten nitride/reduced graphene oxide as a high-performance, non-noble-metal electrocatalyst for the hydrogen evolution reaction. *Angew. Chem., Int. Ed.* **2015**, *54*, 6325–6329.

[34] Wang, Y. Y.; Zhang, Y. Q.; Liu, Z. J.; Xie, C.; Feng, S.; Liu, D. D.; Shao, M. F.; Wang, S. Y. Layered double hydroxide nanosheets with multiple vacancies obtained by dry exfoliation as highly efficient oxygen evolution electrocatalysts. *Angew. Chem., Int. Ed.* **2017**, *56*, 5867–5871.

[35] Peng, J.; Liu, Y. H.; Luo, X.; Wu, J. J.; Lin, Y.; Guo, Y. Q.; Zhao, J. Y.; Wu, X. J.; Wu, C. Z.; Xie, Y. High phase purity of large-sized 1T'-MoS_2 monolayers with 2D superconductivity. *Adv. Mater.* **2019**, *31*, 1900568.

[36] Liu, Z. Y.; Wu, A. P.; Yan, H. J.; Su, D. N.; Jin, C. X.; Guo, H.; Wang, L.; Tian, C. G. An effective "precursor-transformation" route toward the high-yield synthesis of ZIF-8 tubes. *Chem. Commun.* **2020**, *56*, 2913–2916.

[37] Guo, H.; Wu, A. P.; Xie, Y.; Yan, H. J.; Wang, D. X.; Wang, L.; Tian, C. G. 2D porous molybdenum nitride/cobalt nitride heterojunction nanosheets with interfacial electron redistribution for effective electrocatalytic overall water splitting. *J. Mater. Chem. A* **2021**, *9*, 8620–8629.

[38] Lu, X. L.; Xu, K.; Chen, P. Z.; Jia, K. C.; Liu, S.; Wu, C. Z. Facile one step method realizing scalable production of g-C_3N_4 nanosheets and study of their photocatalytic H_2 evolution activity. *J. Mater. Chem. A* **2014**, *2*, 18924–18928.

[39] Xia, P. F.; Zhu, B. C.; Yu, J. G.; Cao, S. W.; Jaroniec, M. Ultra-thin nanosheet assemblies of graphitic carbon nitride for enhanced photocatalytic CO_2 reduction. *J. Mater. Chem. A* **2017**, *5*, 3230–3238.

[40] Yu, Y.; Yan, W.; Wang, X. F.; Li, P.; Gao, W. Y.; Zou, H. H.; Wu, S. M.; Ding, K. J. Surface engineering for extremely enhanced charge separation and photocatalytic hydrogen evolution on g-C_3N_4. *Adv. Mater.* **2018**, *30*, 1705060.

[41] Gao, S. Y.; Wang, X. Y.; Song, C. J.; Zhou, S. J.; Yang, F.; Kong, Y. Engineering carbon-defects on ultrathin g-C_3N_4 allows one-pot output and dramatically boosts photoredox catalytic activity. *Appl. Catal. B Environ.* **2021**, *295*, 120272.

[42] Yu, X. N.; Ng, S. F.; Putri, L. K.; Tan, L. L.; Mohamed, A. R.; Ong, W. J. Point-defect engineering: Leveraging imperfections in graphitic carbon nitride (g-C_3N_4) photocatalysts toward artificial photosynthesis. *Small* **2021**, *17*, 2006851.

[43] Chen, J. J.; Mao, Z. Y.; Zhang, L. X.; Wang, D. J.; Xu, R.; Bie, L. J.; Fahlman, B. D. Nitrogen-deficient graphitic carbon nitride with enhanced performance for lithium ion battery anodes. *ACS Nano* **2017**, *11*, 12650–12657.

[44] Huang, T.; Pan, S. G.; Shi, L. L.; Yu, A. P.; Wang, X.; Fu, Y. S. Hollow porous prismatic graphitic carbon nitride with nitrogen vacancies and oxygen doping: A high-performance visible light-driven catalyst for nitrogen fixation. *Nanoscale* **2020**, *12*, 1833–1841.

[45] Yang, P. J.; Shang, L.; Zhao, J. H.; Zhang, M.; Shi, H.; Zhang, H. X.; Yang, H. Q. Selectively constructing nitrogen vacancy in carbon nitrides for efficient syngas production with visible light. *Appl. Catal. B Environ.* **2021**, *297*, 120496.

[46] Chen, H.; Wang, W. Y.; Yang, Z. Z.; Suo, X.; Lu, Z. Y.; Xiao, W. M.; Dai, S. Alkaline salt-promoted construction of hydrophilic and nitrogen deficient graphitic carbon nitride with highly improved photocatalytic efficiency. *J. Mater. Chem. A* **2021**, *9*, 4700–4706.

[47] Yu, H. J.; Shi, R.; Zhao, Y. X.; Bian, T.; Zhao, Y. F.; Zhou, C.; Waterhouse, G. I. N.; Wu, L. Z.; Tung, C. H.; Zhang, T. R. Alkali-assisted synthesis of nitrogen deficient graphitic carbon nitride with tunable band structures for efficient visible-light-driven hydrogen evolution. *Adv. Mater.* **2017**, *29*, 1605148.

[48] Tian, J. J.; Zhang, L. X.; Fan, X. Q.; Zhou, Y. J.; Wang, M.; Cheng, R. L.; Li, M. L.; Kan, X. T.; Jin, X. X.; Liu, Z. H. et al. A post-grafting strategy to modify g-C_3N_4 with aromatic heterocycles for enhanced photocatalytic activity. *J. Mater. Chem. A* **2016**, *4*, 13814–13821.

[49] Hai, X.; Chang, K.; Pang, H.; Li, M.; Li, P.; Liu, H. M.; Shi, L.; Ye, J. H. Engineering the edges of MoS_2 (WS_2) crystals for direct exfoliation into monolayers in polar micromolecular solvents. *J. Am. Chem. Soc.* **2016**, *138*, 14962–14969.

[50] Li, M. L.; Zhang, L. X.; Fan, X. Q.; Wu, M. Y.; Du, Y. Y.; Wang, M.; Kong, Q. L.; Zhang, L. L.; Shi, J. L. Dual synergetic effects in MoS_2/pyridine-modified g-C_3N_4 composite for highly active and stable photocatalytic hydrogen evolution under visible light. *Appl. Catal. B Environ.* **2016**, *190*, 36–43.

[51] Yan, H. J.; Jiao, Y. Q.; Wu, A. P.; Tian, C. G.; Wang, L.; Zhang, X. M.; Fu, H. G. Synergism of molybdenum nitride and palladium for high-efficiency formic acid electrooxidation. *J. Mater. Chem. A* **2018**, *6*, 7623–7630.

[52] Zhou, W. J.; Yin, Z. Y.; Du, Y. P.; Huang, X.; Zeng, Z. Y.; Fan, Z. X.; Liu, H.; Wang, J. Y.; Zhang, H. Synthesis of few-layer MoS_2 nanosheet-coated TiO_2 nanobelt heterostructures for enhanced photocatalytic activities. *Small* **2013**, *9*, 140–147.

[53] Hou, Y. D.; Laursen, A. B.; Zhang, J. S.; Zhang, G. G.; Zhu, Y. S.;

Wang, X. C.; Dahl, S.; Chorkendorff, I. Layered nanojunctions for hydrogen-evolution catalysis. *Angew. Chem., Int. Ed.* **2013**, *52*, 3621–3625.

[54] Zhou, W. W.; Liu, M. F.; Zhang, Q.; Wei, Q.; Ding, S. J.; Zhou, Y. S. Synthesis of NiMo catalysts supported on gallium-containing mesoporous Y zeolites with different gallium contents and their high activities in the hydrodesulfurization of 4, 6-dimethyldibenzothiophene. *ACS Catal.* **2017**, *7*, 7665–7679.

[55] Wu, A. P.; Tian, C. G.; Jiao, Y. Q.; Yan, Q.; Yang, G. Y.; Fu, H. G. Sequential two-step hydrothermal growth of MoS_2/CdS core–shell heterojunctions for efficient visible light-driven photocatalytic H_2 evolution. *Appl. Catal. B Environ.* **2017**, *203*, 955–963.

[56] Zhu, J. T.; Xu, H.; Zou, G. F.; Zhang, W.; Chai, R. Q.; Choi, J.; Wu, J.; Liu, H. Y.; Shen, G. Z.; Fan, H. Y. MoS_2–OH bilayer-mediated growth of inch-sized monolayer MoS_2 on arbitrary substrates. *J. Am. Chem. Soc.* **2019**, *141*, 5392–5401.

[57] Midya, A.; Ghorai, A.; Mukherjee, S.; Maiti, R.; Ray, S. K. Hydrothermal growth of few layer 2H-MoS_2 for heterojunction photodetector and visible light induced photocatalytic applications. *J. Mater. Chem. A* **2016**, *4*, 4534–4543.

[58] Sun, B. J.; Zhou, W.; Li, H. Z.; Ren, L. P.; Qiao, P. Z.; Li, W.; Fu, H. G. Synthesis of particulate hierarchical tandem heterojunctions toward optimized photocatalytic hydrogen production. *Adv. Mater.* **2018**, *30*, 1804282.